Biophysical Reports, Volume *1*

Supplemental information

Surface tension and viscosity of protein condensates quantified by micropipette aspiration

Huan Wang, Fleurie M. Kelley, Dragomir Milovanovic, Benjamin S. Schuster, and Zheng Shi

Materials and Methods

Estimate of the working range of MPA through dimensional analysis

In this study, we assume that condensates behave as Newtonian fluids. During micropipette aspiration of the condensate (Fig. 2a), the viscosity needs to be large in order for the camera to capture the flow process. At the same time, the surface tension needs to be small in order for the flow to start.

Assume the maximal imaging frequency is 100 Hz ($\Delta t_{\min}$ = 0.01 s), the radius of the pipette is R_p = 1 μm, and M = 500 (see Equation 1 in the main text). In order to capture liquid deformations that are on the order of pipette diameter (ΔL_p = 2 μm), the viscosity η (in Pa·s) needs to satisfy:

$$\eta > |P_{\mathrm{asp}}| \cdot \frac{R_{\mathrm{p}} \Delta t_{\min}}{M \Delta L_{\mathrm{p}}} = 10^{-5} |P_{\mathrm{asp}}| \qquad \text{(S1)}$$

The aspiration pressure needs to overcome the capillary effect caused by the surface tension γ (in mN/m). For a non-wetting ($H^{-1} = R_p$) or a perfectly wetting ($H^{-1} = -R_p$) liquid with $R_c >> R_p$:

$$|P_{\mathrm{asp}}| > \frac{2\gamma}{R_{\mathrm{p}}} = 2 \times 10^{3} \gamma \qquad \text{(S2)}$$

Combine relations S1 and S2:

$$\eta(\text{in Pa} \cdot \text{s}) > 2 \times 10^{-2}\ \gamma\ (\text{in mN/m}) \qquad \text{(S3)}$$

Therefore, relation S3 defines the regime of viscosity and surface tension where MPA is expected to perform well. In Fig. 1, η = 0.02 γ is plotted as the black dashed line, the gray region represents η = 0.01 γ ~ 0.04 γ.

Protein purification and sample preparation

RGG-based proteins were expressed recombinantly in *E. coli* and purified by affinity chromatography, as previously described *(1)*. The working protein sample contains 1 μM RGG-EGFP-RGG (molecular mass 62.1 kDa, Addgene Plasmid #124948) and 6 μM RGG-RGG (molecular mass 35.7 kDa, Addgene Plasmid #124941) in a pH 7.5 buffer containing 20 mM Tris and 150 mM NaCl.

Phase separated dextran and PEG aqueous two-phase systems were prepared by mixing different concentrations of PEG-8000 (43443-22, Alfa Aesar, US) and dextran-500k (DE132-100GM, Spectrum Chemical, US) stock solutions. The stock solutions were prepared by dissolving each polymer in Milli-Q water. Emulsions of different PEG to dextran ratios showed different distributions of droplet size (Fig. S1a). The 5% PEG and 6.4% dextran (both by mass) mixture was chosen for micropipette aspiration, because the resulting emulsion contained droplets with comparable sizes to those of the protein condensates.

Rhodamine-B (83689-1G, Sigma, USA) was added (at a final concentration of 1 μM) to the PEG-dextran mixture to distinguish the dextran phase from the PEG phase (Fig. 2b). Rhodamine-B preferentially enters the PEG-rich phase *(2)*, therefore dextran-rich condensates showed as dark droplets in a bright background in fluorescent microscopy images (Fig. 2b, upper right image). The fluorescent labeling was confirmed by the observation that after bulk LLPS, the heavier dextran-rich layer (Fig. 2b, lower layer of the lower left image) contained less Rhodamine-B compared to the lighter PEG-rich layer. The concentration of dextran in the dextran-rich layer was estimated to be ~14% by mass.

Micropipette fabrication, aspiration, and imaging

Micropipettes were pulled from glass capillaries using a pipette puller (PUL-1000, World Precision Instruments (WPI), US). The tip of the pipette was cut to an opening diameter between 1~ 5 μm and bent to ~40° using a microforge (DMF1000, WPI).

Micropipette aspiration and imaging were carried out on a Ti2-A inverted fluorescent microscope (Nikon, Japan) equipped with a motorized stage and two motorized 4-axes micromanipulators (PatchPro-5000, Scientifica, UK). A micropipette was filled with the same buffer as the protein (20 mM Tris and 150 mM NaCl, pH 7.5) using a MICROFIL needle (WPI) and subsequently mounted onto a micromanipulator. The rear end of the pipette was connected to an adjustable water reservoir. The pipette holder was then rotated so that the bent tip of the micropipette was parallel to the imaging plane. The aspiration pressure within the micropipette was controlled and recorded by adjusting the water level in the reservoir using a set of 5 ml, 20 ml, 50 ml, and 150 ml syringes connected to the reservoir.

The zero pressure of the system was calibrated before each MPA experiment, using a dilute solution of fluorescent nanoparticles. The zero pressure (P_0) was set according to the point where fluorescent nanoparticles underwent Brownian motion inside the micropipette. The error in aspiration pressure (<2 Pa) was defined as the minimal pressure change near P_0 that resulted in an observable directed flow of fluorescent particles in the micropipette.

MPA experiments were carried out in glass-bottom dishes (ES56291, Azer Scientific, US) that were pre-treated with 5% Pluronic F-127 (P2443-250G, Sigma) for > 1 hour to prevent adhesion of RGG condensates to the glass*(1)*. Milli-Q water was added to the edge of the dish to minimize evaporation from the sample (Fig. 2a). We further quantified water evaporation rates under our experimental conditions using a 20 µL sample of Rhodamine-B solution (Fig. S2). Volume of the sample was assumed to be inversely proportional to its mean fluorescence intensity. No measurable volume change was observed when the dish-cap was on, providing a stable environment for necessary incubation periods for the sample. When the dish-cap was removed for micropipette aspiration, evaporation led to a slow constant decrease in the sample volume (~0.04 µL/min). We found that the evaporation can be compensated to be less than 5% in our MPA experiments (Fig. S2).

After calibration of the aspiration pressure, a 20~30 μL sample of phase separated protein solution was added to the center of the dish (Fig. 2a). Once micrometer-size protein condensates were observed at the bottom of the dish, a calibrated micropipette was moved to a condensate of interest to start the aspiration measurements. First, a positive (suction) pressure was applied to initiate the flow of the condensate into the micropipette. The condensate was typically allowed to flow into the micropipette until the aspiration length reached ~40 μm (the maximal aspiration length was limited by the field of view of the camera, initial condensate size, and the exact angle of the micropipette tip). Then, sequential stepwise ejection and suction pressures were applied to deform the condensate at different shear stresses while maintaining the aspiration length to be between 5 to 40 μm (Fig. 3b and S3a-b). The deformation of the condensate was recorded using a 60X objective, at 1 Hz (ORCA-Flash 4.0, Hamamatsu, Japan), either through transmitted light imaging (Fig. S1, S4, Movie S3) or through imaging the fluorescence of the EGFP tag (Fig. 3, S3, Movies S1, S2). The shape parameters of the aspirated condensates (L_p, R_p, R_c, H) were tracked using ImageJ. For data collected in the fluorescent channel, a MATLAB (R2019a) code was developed to automate the tracking of L_p. In the case of pipette-adhered condensates, we used the shape of the non-adherent part as an approximate for R_c.

To neglect potential nonlinear effect due to dissipation of the condensate flow in the pipette, the volume of condensate inside the micropipette is always around or below 5% of the volume of condensate outside the pipette. Larger condensates also lead to more accurate MPA measurements, because of the smaller perturbation of the changing aspiration length to R_c. For a condensate that is larger than 10 μm in radius, typical changes in aspiration length correspond to a < 3% change in R_c. For these reasons, in our experiments, small condensates were first manipulated into a large condensate through either a micropipette or an optical trap (see "**Optical trap mediated condensate fusion**" section) before MPA measurements.

When the RGG condensate first entered the micropipette, wetting between protein and glass led to dramatic changes in the interfacial curvature between the condensate and buffer inside the micropipette. The interfacial curvature stabilized in later steps (Fig. S3a, Movie S1). As a result, the P_{asp} vs. S relation during the initial-entry largely deviated from that of the remaining steps (Fig. S3b, S3c). We corrected for the change in H by subtracting a time-dependent P_γ from the aspiration pressure (Fig. S3d). However, the irreversible binding of a trace amount of protein to the inner wall of the aspiration pipette significantly accelerated the deformation of condensates during the initial-entry steps (Fig. S3e, S3f). To account for the lack of information about the kinetics of protein-glass binding, we disregarded the measurements from the initial-entry steps.

After the initial steps, the interfacial curvature between RGG condensates and buffer in the micropipette was set by the wetting of the protein to the inner pipette wall (Movie S1). Due to this wetting effect, RGG condensates flowed into the micropipette under both positive (suction) and small negative (ejection) pressures, whereas decreases in aspiration length only happened under large negative (ejection) pressures (Fig. 3, Movie S1, Fig. S4).

Viscosity of dextran-rich condensates

To calibrate the viscosity measurements, MPA should be applied to condensates with viscosity values that can be easily determined through other means. Dextran-rich condensates in a PEG-dextran aqueous two-phase system were chosen for this purpose (Fig. 2). After MPA, two independent methods were used to measure the viscosity of the dextran-rich phase.

1. Optical dragging

   An optical trap (Tweez305, Aresis, Slovenia) was applied to drag an r = 1.60 μm radius polystyrene bead (HUP-30-5, Spherotech, US) in a large dextran-rich condensate at 13 different velocities (Fig. 2e). The slope of the dragging force (f) vs. dragging speed (v) was used to calculate the viscosity (η) based on the Stokes equation (Equation S4):

$$\frac{df}{dv} = \eta \cdot 6\pi r \qquad \text{(S4)}$$

The measured viscosity was 74 ± 4 mPa·s. The stiffness of the optical trap (~ 0.02 pN/nm) was calibrated before each experiment by applying equipartition theorem to the thermal fluctuation of a trapped bead in the dextran-rich phase *(3)*.

2. Ubbelohde viscometer

After the bulk-phase separation of 40 ml PEG-dextran mixture, the bottom layer, corresponding to the dextran-rich phase, was applied through an Ubbelohde viscometer (13-614C, Cannon Instrument, US). The viscosity was measured to be 80 mPa·s.

Optical trap mediated condensate fusion

Two RGG condensates were individually controlled by two independent optical traps (Tweez305, Aresis, Slovenia) equipped on the Ti2-A inverted microscope (Nikon, Japan). As illustrated in Fig. 4a, the right condensate was moved towards the left one until they touched. Then, the right optical trap was turned off, and the condensates were allowed to fuse under the combined influence of their viscosity and surface tension. The fusion processes were acquired at a frame rate of 20 Hz using a 60x water objective. The acquired images were analyzed in MATLAB. The images were fitted into a Gaussian ellipse and the ratio of the major to minor axes of the ellipse (aspect ratio) was plotted as a function of time. The fusion time (τ) was extracted by fitting the change in the aspect ratio (*AR*) of fusing condensates to a single exponential decay (Fig. 4b, Equation S5).

$$AR = 1 + (AR_0 - 1)\mathrm{e}^{-t/\tau} \qquad \text{(S5)}$$

The length of condensates was defined as the geometric mean of the condensate diameters before fusion *(4)*. The ratio of viscosity to surface tension (inverse capillary velocity) was estimated from the slope of the fusion time vs. length relation (Fig. 4c).

Here, we chose the simple exponential fitting (eq. S5) to be consistent with the commonly-used routine in the literature *(4-9)*. We noticed that a stretched-exponential equation $AR = 1 + (AR_0 - 1)\mathrm{e}^{(-t/\tau)^{1.5}}$ can marginally improve the fitting quality to our fusion kinetics data (Fig. 4b), similar to the observation in a recent study *(10)*. The fitted fusion time τ, and therefore the inverse capillary velocity, were not significantly different from the values presented in Fig. 4c.

FRAP measurement of the condensate viscosity

FRAP experiments were performed on a total internal reflection fluorescence microscope (DMi8 TIRF, Leica, Germany) equipped with an Infinity Scanner system (Leica, Germany). All images were acquired using a 100X oil objective at 1 Hz. A 1.5 μm radius circular region was photobleached at the center of large RGG condensates (radius 9 ± 2 μm) using a short pulse (~1 s) of focused 488 nm laser, and the fluorescence recovery was analyzed using ImageJ. After background subtraction, fluorescence of the bleached region (I_{ROI}) was divided by the fluorescence of the entire condensate (I_{cond}) according to Equation S6, to minimize photobleaching and boundary effects *(11, 12)*.

$$I(t) = \frac{I_{ROI}(t) - I_{background}(t)}{I_{cond}(t) - I_{background}(t)} \qquad \text{(S6)}$$

The time point right after the bleaching step was defined as time zero. $I(t)$ was normalized so that the average of $I(t < 0)$ equals to 1.

To extract the half-recovery time, $I(t)$ was fitted to Equation S7a or Equation S7b, depending on whether an immobile fraction was included in the model.

$$I(t) = \frac{I_0 + I_\infty \frac{t}{\tau_{1/2}}}{1 + \frac{t}{\tau_{1/2}}} \qquad \text{(S7a)}$$

$$I(t) = \frac{I_0 + \frac{t}{\tau_{1/2}}}{1 + \frac{t}{\tau_{1/2}}} \qquad \text{(S7b)}$$

Here, $\tau_{1/2}$ is the half-recovery time and I_∞ is the mobile fraction (in Equation S7b, I_∞ is set to 1). For the FRAP measurements in this study (Fig. 4d), $\tau_{1/2}$ = 12.4 ± 0.5 s and I_∞ = 0.928 ± 0.003 when fitted to Equation S7a, while $\tau_{1/2}$ = 24 ± 1 s, when fitted to Equation S7b. Fittings were carried out in OriginPro 2020.

The diffusion coefficient (*D*) of the bleached molecule (RGG-EGFP-RGG) can be determined from a 2D or a 3D infinity model, according to Equation S8a or S8b, respectively *(11)*.

$$D = \frac{0.22 \cdot {r_{ROI}}^2}{\tau_{1/2}} \qquad \text{(S8a)}$$

$$D = \frac{0.1 \cdot {r_{ROI}}^2}{\tau_{1/2}} \qquad \text{(S8b)}$$

Where r_{ROI} = 1.5 μm is the radius of the bleached area, $\tau_{1/2}$ is the recovery time from Equation S7.

The viscosity of RGG condensates was then calculated using the Stokes-Einstein relation (Equation S9).

$$\eta = \frac{k_B T}{6\pi R_H D} \qquad \text{(S9)}$$

R_H is the hydrodynamic radius of RGG-EGFP-RGG. Using the online Hydrodynamic Radius Converter (https://www.fluidic.com/resources/Toolkit/hydrodynamic-radius-Converter/), R_H was estimated to be 6.54 nm, by taking into consideration the molecular mass and folding of RGG-GFP-RGG*(13)*.

Data availability

MATLAB codes used for quantitative data analysis in this study are available upon request.

Supplementary Figures

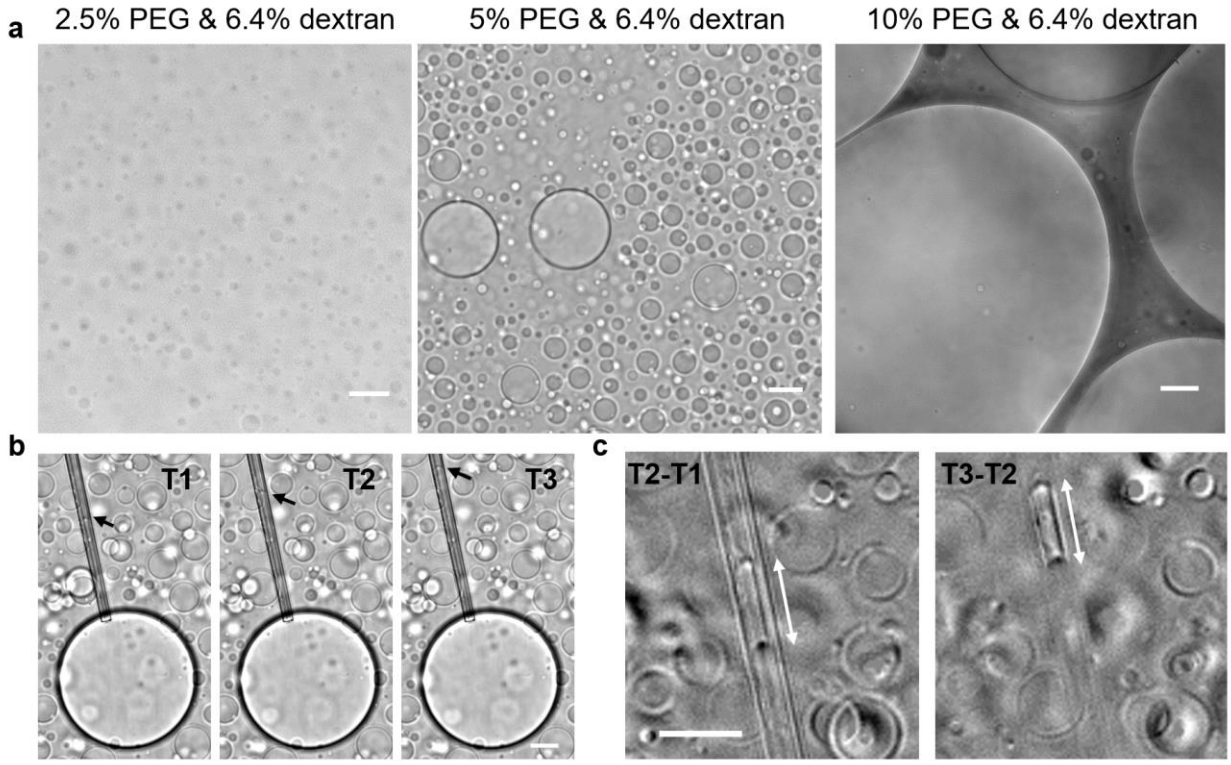

Figure S1: Phase separation and micropipette aspiration analysis of PEG and Dextran mixtures.
a, Micrometer-scale droplets were observed in emulsions of PEG-dextran. Left to right: mixtures of PEG (8,000 Da) and dextran (500,000 Da) at increasing ratios of PEG to dextran. The 5% PEG & 6.4% dextran condition was chosen to produce droplets with similar sizes to those of protein condensates. **b**, Flow of a dextran-rich condensate into a micropipette (pre-filled with PEG-rich solution) under constant suction pressure (60 Pa). The 3 images were taken at 3 seconds apart. Arrows point to the interfaces between the dextran-rich and PEG-rich phases which are zoomed-in in **c**. **c**, Intensity differences between images in **b**: T2-T1 (left) and T3-T2 (right). The double-arrows show the increase of aspiration length in 3 seconds. Analysis of the MPA experiment can be achieved as long as the condensate-buffer interface is resolvable. All scale bars, 20 µm.

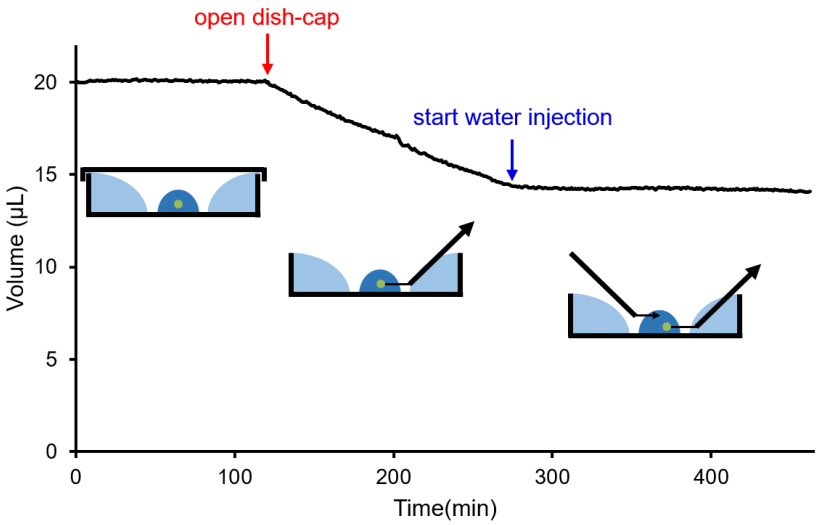

Figure S2: Quantification and correction of water evaporation during micropipette aspiration experiments.
Under our experimental conditions, the presence of peripheral water eliminated evaporation from the 20 µL sample as long as the cap of sample dish was on. Upon removing the cap (red arrow) for micropipette aspiration, water slowly evaporated at a rate of 0.04 µL/min. The evaporation during micropipette aspiration was compensated (blue arrow) through continuous injection of pure water using a second micropipette, or by adding 2 µL of pure water every 50 min. Sample volume was measured through fluorescence-based concentration measurement of Rhodamine-B at an imaging rate of 1 frame per minute and no measurable photobleaching was observed.

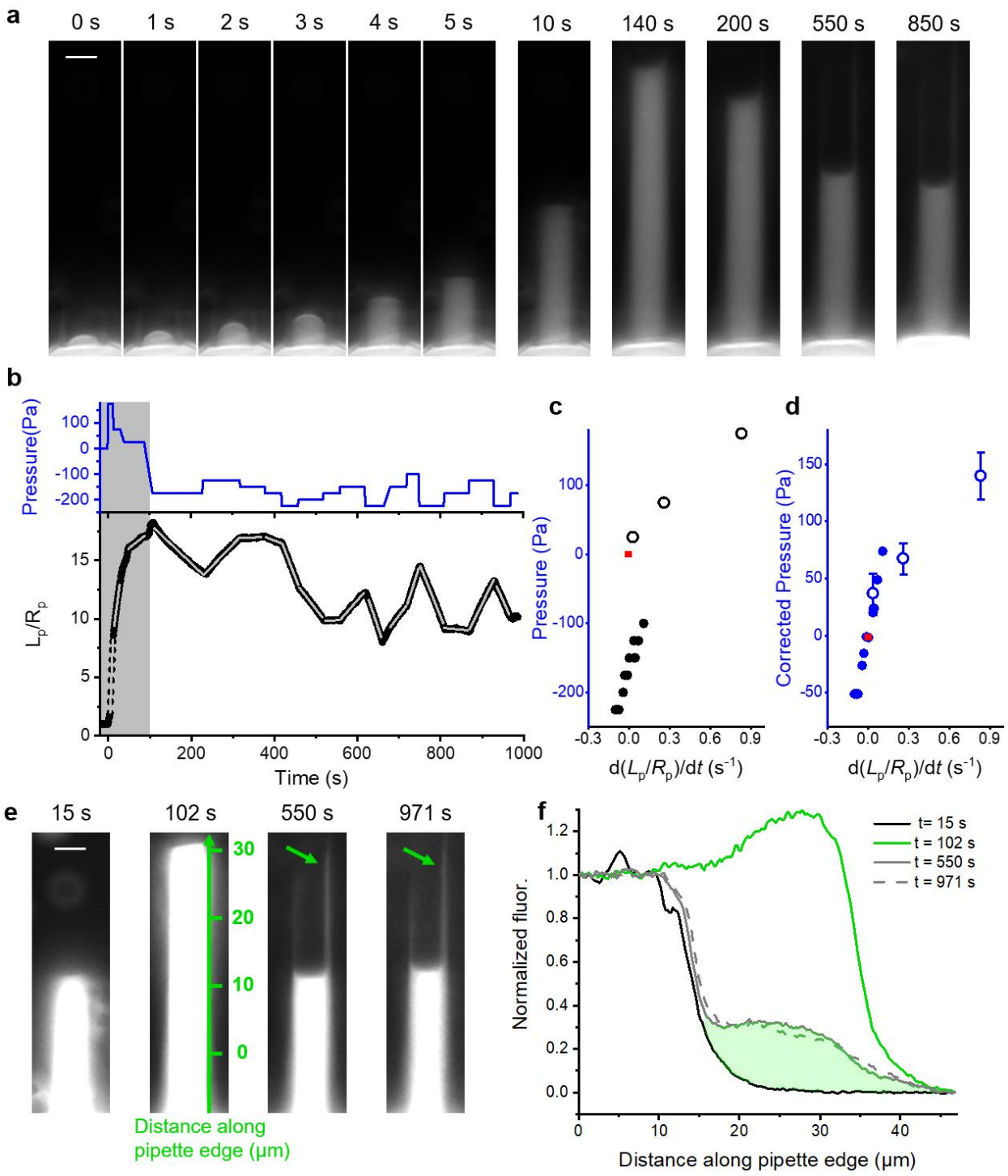

Figure S3: The interfacial curvature and the wetting of RGG condensate inside micropipette.

a, Time lapse fluorescence images showing the aspirated portion of the condensate. After proteins enter the micropipette (1- 4 s), the wetting of proteins to the inner pipette wall led to swift changes in the interfacial curvature of the protein condensate. In the case of RGG, this curvature stabilized within 2 min and remained near -1/R_p in the following aspiration steps. **b**, Aspiration

pressure (upper) and normalized aspiration length (lower) as a function of time. Shaded area represents the initial-entry steps (defined as when the protein condensate first encountered a bare glass micropipette), where irreversible binding of protein to pipette inner wall happens. Gray lines are linear fits to the normalized aspiration length under each pressure step. **c-d**, Raw aspiration pressure (**c**) and tension-corrected pressure (**d**) of each step plotted against the normalized deformation rate (slopes of the gray lines in **b**). The initial-entry steps are denoted by open circles and a red square is placed at (0,0). Error bars in **d** reflect the uncertainty in interfacial curvature during the initial-entry steps. **e**, Over-exposed images of the aspirated portion during (15 s, 102 s) and after (550 s, 971 s) the initial-entry steps. The axis (at 102 s) represents the edge of the micropipette, arrow (at 550 s) points to proteins that were stuck to the inner pipette wall, which persisted in further aspiration steps (arrow at 971 s). **f**, Line profile along the pipette edge at the four time points shown in **e**. Area of the shaded region shows the amount of protein that was stuck on the inner wall of the micropipette. All scale bars, 5 μm.

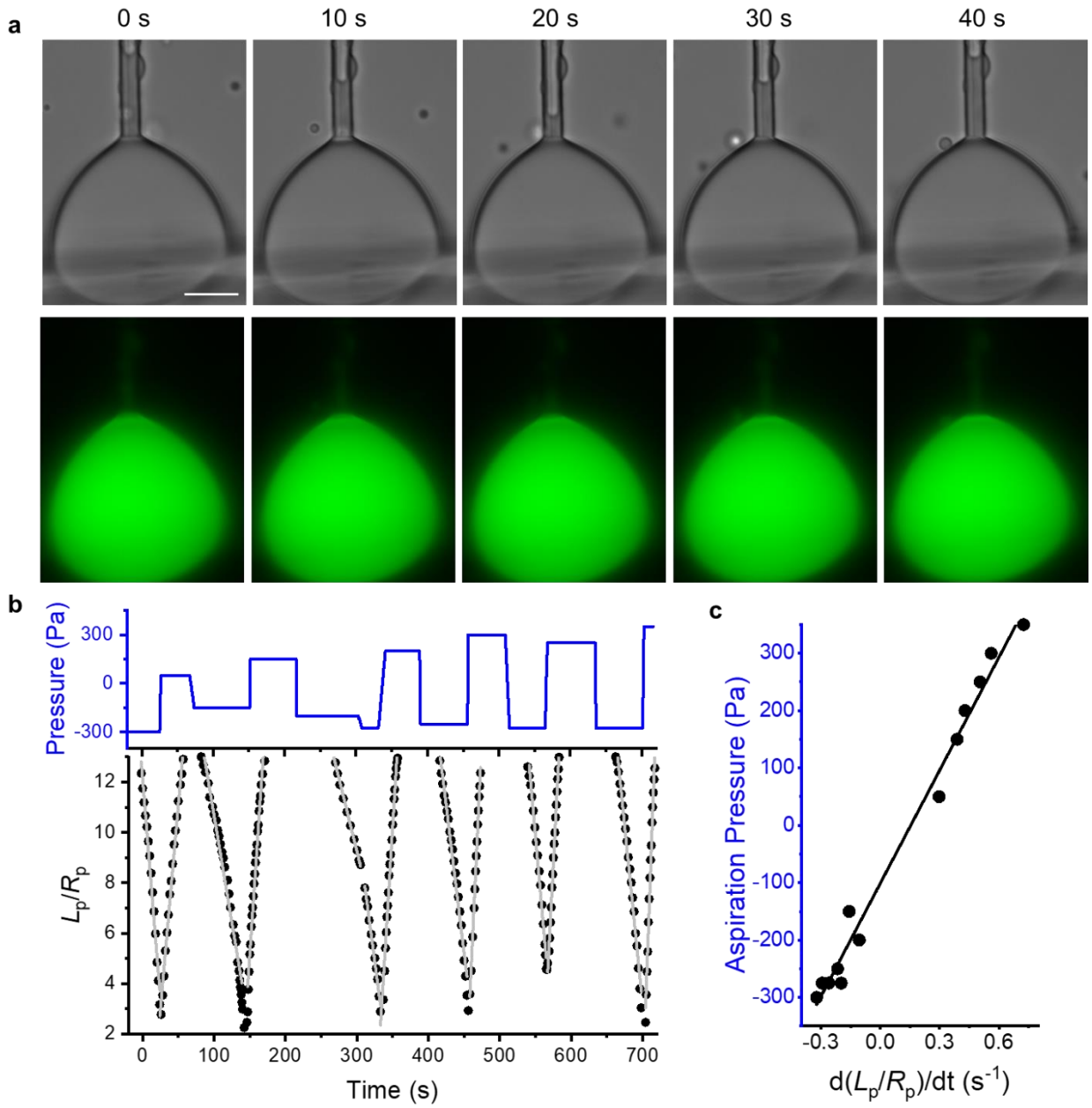

Figure S4: Micropipette aspiration analysis of RGG condensates under transmitted light. **a**, Time lapse transmitted (upper) and fluorescence (lower) images of an RGG condensate (adhered to a second pipette) under sequential ejection (-300 Pa, 0~20 s) and suction pressures (50 Pa, 20~40 s). **b**, Aspiration pressure (upper) and normalized aspiration length (lower) quantified from the transmitted light images. Gray lines: linear fits of the normalized aspiration length for each pressure step. **c**, P_{asp} of each step plotted against V (slopes of the gray lines in **b**). The black line represents a linear fit (slope: 660 ± 30 Pa·s, intercept: -100 ± 10 Pa, $R^2 = 0.985$). Scale bars, 10 µm.

Captions for Supplementary Movies

Movie S1: Micropipette aspiration of an RGG condensate free from adhesion to glass surfaces.

Movie S2: Micropipette aspiration of an RGG condensate strongly adhered to a glass pipette.

Movie S3: Micropipette aspiration of an RGG condensate imaged with transmitted light.

Supplementary Table

Liquid condensate	Viscosity (Pa·s) and method	Surface tension (mN/m) and method	Note
PGL-1*(4)*	~1 FRAP	~10^{-3} Fusion	Order of magnitude estimates
LAF-1*(14)*	23.4 SPT	0.19 Fusion	Average over RNA concentrations
Whil3*(15)*	15 FRAP and SPT	5 x 10^{-5} Fusion	Average over RNA concentrations
NPM1*(6)*	0.74 FRAP and SPT	8 x 10^{-4} Fusion and Sessile drop	
NPM1(*in vivo*) *(6)*	37 FRAP	4 x 10^{-4} Fusion and Sessile drop	
FIB1*(6)*	100 FRAP and SPT	1.23 x 10^{-3} Fusion and Sessile drop	
PGL-3*(16, 17)*	1 to 10^{4} Dual-OT	~4.5 x 10^{-3} Dual-OT	The viscosity increased significantly over time
FUS*(16)*	0.7 to 50 Dual-OT	~3.1 x 10^{-3}* Dual-OT	The viscosity increased significantly over time
Poly K*(18)*	0.204 FRAP and SPT	0.017 Fusion	
Poly R*(18)*	14.4 FRAP and SPT	0.1 Fusion	
[RGRGG]$_5$-dT40*(8)*	3 SPT and FCS	0.8 Fusion-OT	Average over salt concentrations
Glycinin*(19)*	~1600 Fusion	~0.16 Estimate	Surface tension $\gamma \sim k_B T/d^2$, where d is the size of glycinin
Cell Nucleus*(20)*	3000 Surface fluctuation	1.5 x 10^{-3} Fusion	
Double-Hydrophilic Block Copolymers*(21)*	*0.004* *FRAP*	*~5 x 10^{-5}* *Fusion*	*Not included in the plot of Figure 1*
Dextran-PEG*(22-24)*	0.023~0.17 Viscometer	0.01~0.1 Pendant drop Spinning drop tensiometer	At compositions similar to sample used in this study
Olive oil*(25, 26)*	0.0741 Viscometer	23.6 Pendent drop	All measured in water
Silicon oil*(27)*	0.02 Viscometer	36 Bubble contour	
Mineral oil*(28)*	7.75 x 10^{-3} Viscometer	49 Tensiometer	
$C_{16}H_{34}$ *(29)*	2.77 x 10^{-3} Viscometer	55.2 Tensiometer	
$C_{16}H_{34}$ with surfactants*(30)*	Assumed to be the same as above	Lowest to ~ 0.3 Tensiometer	
$C_{10}H_{22}$ *(29)*	9 x 10^{-4} Viscometer	53.2 Tensiometer	
C_6H_{14} *(29)*	3.13 x 10^{-4} Viscometer	51.4 Tensiometer	

Table S1: Literature values, methods, and references for data presented in Figure 1
FRAP: fluorescence recovery after photobleaching. **SPT**: single particle tracking. **Fusion**: first, a ratio of surface tension to viscosity was estimated from the fusion kinetics between two condensates. Then, a separate measure of viscosity was used to calculate surface tension values. Fusion experiments carried out using optical traps were noted as Fusion-OT. **Sessile drop**: a prism was used to image condensates

of various sizes from the side. The shape is determined by surface tension and gravity of the condensate. A separate measure of condensate density was used to extract surface tension. **Dual-OT**: Dual optical traps were used to periodically stretch a condensate via two bead-handles. Viscoelasticity of the condensate was measured via the phase delay of the strain relative to the stress. Surface tension was estimated from the elasticity of condensates.
** Surface tension value of FUS condensates was kindly provided by Dr. Frank Jülicher via email*

Supporting References

1. Schuster, B. S.; Reed, E. H.; Parthasarathy, R.; Jahnke, C. N.; Caldwell, R. M.; Bermudez, J. G.; Ramage, H.; Good, M. C.; Hammer, D. A. Controllable protein phase separation and modular recruitment to form responsive membraneless organelles. *Nature communications* **2018***, 9*, 1-12.

2. Riedstra, C. P.; McGorty, R. Liquid–Liquid Phase Separation: Undergraduate Labs on a New Paradigm for Intracellular Organization. *The Biophysicist* **2020***, 1*.

3. Osterman, N. TweezPal–optical tweezers analysis and calibration software. *Comput. Phys. Commun.* **2010***, 181*, 1911-1916.

4. Brangwynne, C. P.; Eckmann, C. R.; Courson, D. S.; Rybarska, A.; Hoege, C.; Gharakhani, J.; Jülicher, F.; Hyman, A. A. Germline P granules are liquid droplets that localize by controlled dissolution/condensation. *Science* **2009***, 324*, 1729-1732.

5. Brangwynne, C. P.; Mitchison, T. J.; Hyman, A. A. Active liquid-like behavior of nucleoli determines their size and shape in Xenopus laevis oocytes. *Proceedings of the National Academy of Sciences* **2011***, 108*, 4334-4339.

6. Feric, M.; Vaidya, N.; Harmon, T. S.; Mitrea, D. M.; Zhu, L.; Richardson, T. M.; Kriwacki, R. W.; Pappu, R. V.; Brangwynne, C. P. Coexisting liquid phases underlie nucleolar subcompartments. *Cell* **2016***, 165*, 1686-1697.

7. Agudo-Canalejo, J.; Schultz, S. W.; Chino, H.; Migliano, S. M.; Saito, C.; Koyama-Honda, I.; Stenmark, H.; Brech, A.; May, A. I.; Mizushima, N.; Knorr, R. L. Wetting regulates autophagy of phase-separated compartments and the cytosol. *Nature* **2021***, 591*, 142-146.

8. Alshareedah, I.; Thurston, G. M.; Banerjee, P. R. Quantifying viscosity and surface tension of multicomponent protein-nucleic acid condensates. *Biophys. J.* **2021**.

9. Schuster, B. S.; Dignon, G. L.; Tang, W. S.; Kelley, F. M.; Ranganath, A. K.; Jahnke, C. N.; Simpkins, A. G.; Regy, R. M.; Hammer, D. A.; Good, M. C. Identifying sequence perturbations to an intrinsically disordered protein that determine its phase-separation behavior. *Proceedings of the National Academy of Sciences* **2020***, 117*, 11421-11431.

10. Ghosh, A.; Zhou, H. Determinants for Fusion Speed of Biomolecular Droplets. *Angewandte Chemie International Edition* **2020***, 59*, 20837-20840.

11. Taylor, N. O.; Wei, M.; Stone, H. A.; Brangwynne, C. P. Quantifying dynamics in phase-separated condensates using fluorescence recovery after photobleaching. *Biophys. J.* **2019***, 117*, 1285-1300.

12. Shi, Z.; Graber, Z. T.; Baumgart, T.; Stone, H. A.; Cohen, A. E. Cell membranes resist flow. *Cell* **2018***, 175*, 1769-1779. e13.

13. Armstrong, J. K.; Wenby, R. B.; Meiselman, H. J.; Fisher, T. C. The hydrodynamic radii of macromolecules and their effect on red blood cell aggregation. *Biophys. J.* **2004***, 87*, 4259-4270.

14. Elbaum-Garfinkle, S.; Kim, Y.; Szczepaniak, K.; Chen, C. C.; Eckmann, C. R.; Myong, S.; Brangwynne, C. P. The disordered P granule protein LAF-1 drives phase separation into droplets with tunable viscosity and dynamics. *Proceedings of the National Academy of Sciences* **2015***, 112*, 7189-7194.

15. Zhang, H.; Elbaum-Garfinkle, S.; Langdon, E. M.; Taylor, N.; Occhipinti, P.; Bridges, A. A.; Brangwynne, C. P.; Gladfelter, A. S. RNA controls PolyQ protein phase transitions. *Mol. Cell* **2015***, 60*, 220-230.

16. Jawerth, L.; Fischer-Friedrich, E.; Saha, S.; Wang, J.; Franzmann, T.; Zhang, X.; Sachweh, J.; Ruer, M.; Ijavi, M.; Saha, S.; Mahamid, J.; Hyman, A. A.; Jülicher, F. Protein condensates as aging Maxwell fluids. *Science* **2020***, 370*, 1317-1323.

17. Jawerth, L. M.; Ijavi, M.; Ruer, M.; Saha, S.; Jahnel, M.; Hyman, A. A.; Jülicher, F.; Fischer-Friedrich, E. Salt-dependent rheology and surface tension of protein condensates using optical traps. *Phys. Rev. Lett.* **2018***, 121*, 258101.

18. Fisher, R. S.; Elbaum-Garfinkle, S. Tunable multiphase dynamics of arginine and lysine liquid condensates. *Nature Communications* **2020***, 11*, 1-10.

19. Chen, N.; Zhao, Z.; Wang, Y.; Dimova, R. Resolving the Mechanisms of Soy Glycinin Self-Coacervation and Hollow-Condensate Formation. *ACS Macro Letters* **2020***, 9*, 1844-1852.

20. Caragine, C. M.; Haley, S. C.; Zidovska, A. Surface fluctuations and coalescence of nucleolar droplets in the human cell nucleus. *Phys. Rev. Lett.* **2018***, 121*, 148101.

21. Lira, R. B.; Willersinn, J.; Schmidt, B. V.; Dimova, R. Selective Partitioning of (Biomacro) molecules in the Crowded Environment of Double-Hydrophilic Block Copolymers. *Macromolecules* **2020***, 53*, 10179-10188.

22. Atefi, E.; Mann Jr, J. A.; Tavana, H. Ultralow interfacial tensions of aqueous two-phase systems measured using drop shape. *Langmuir* **2014***, 30*, 9691-9699.

23. Carrasco, F.; Chornet, E.; Overend, R. P.; Costa, J. A generalized correlation for the viscosity of dextrans in aqueous solutions as a function of temperature, concentration, and molecular weight at low shear rates. *J Appl Polym Sci* **1989***, 37*, 2087-2098.

24. Liu, Y.; Lipowsky, R.; Dimova, R. Concentration dependence of the interfacial tension for aqueous two-phase polymer solutions of dextran and polyethylene glycol. *Langmuir* **2012***, 28*, 3831-3839.

25. Fisher, L. R.; Mitchell, E. E.; Parker, N. S. Interfacial tensions of commercial vegetable oils with water. *J. Food Sci.* **1985***, 50*, 1201-1202.

26. Sahasrabudhe, S. N.; Rodriguez-Martinez, V.; O'Meara, M.; Farkas, B. E. Density, viscosity, and surface tension of five vegetable oils at elevated temperatures: Measurement and modeling. *Int. J. Food Prop.* **2017***, 20*, 1965-1981.

27. Peters, F.; Arabali, D. Interfacial tension between oil and water measured with a modified contour method. *Colloids Surf. Physicochem. Eng. Aspects* **2013***, 426*, 1-5.

28. Kim, H.; Burgess, D. J. Prediction of interfacial tension between oil mixtures and water. *J. Colloid Interface Sci.* **2001***, 241*, 509-513.

29. Goebel, A.; Lunkenheimer, K. Interfacial tension of the water/n-alkane interface. *Langmuir* **1997***, 13*, 369-372.

30. Chen, H.; Han, L.; Luo, P.; Ye, Z. The interfacial tension between oil and gemini surfactant solution. *Surf. Sci.* **2004***, 552*, L53-L57.